# Supplementary Material

## Appendix A Additional Figures and Tables

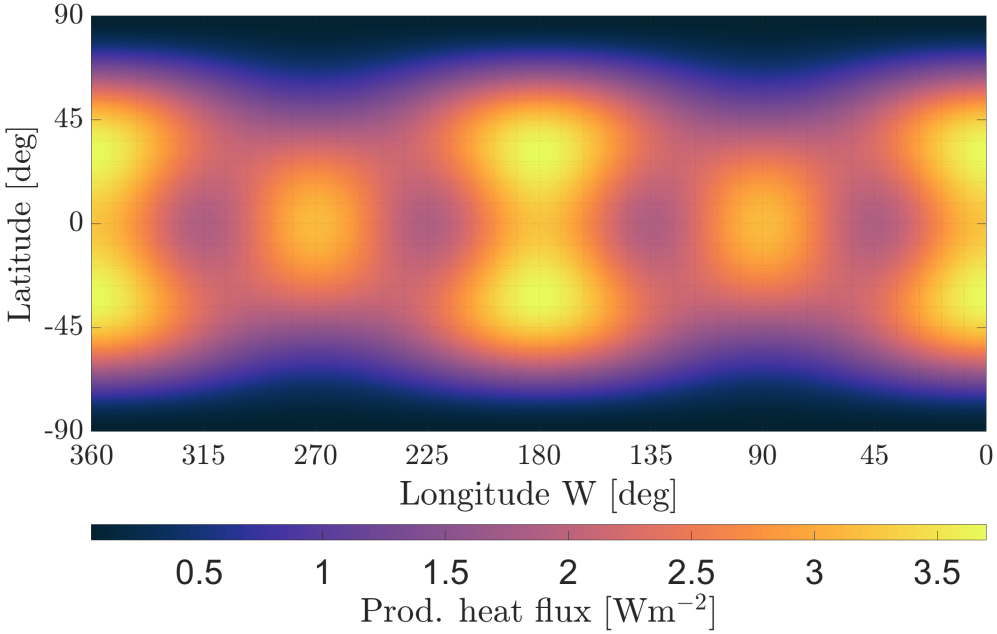


**Fig. A1** Surface heat flux for a uniform Io with solid-body dissipation in the asthenosphere. The map is centered on the anti-subjovian point.

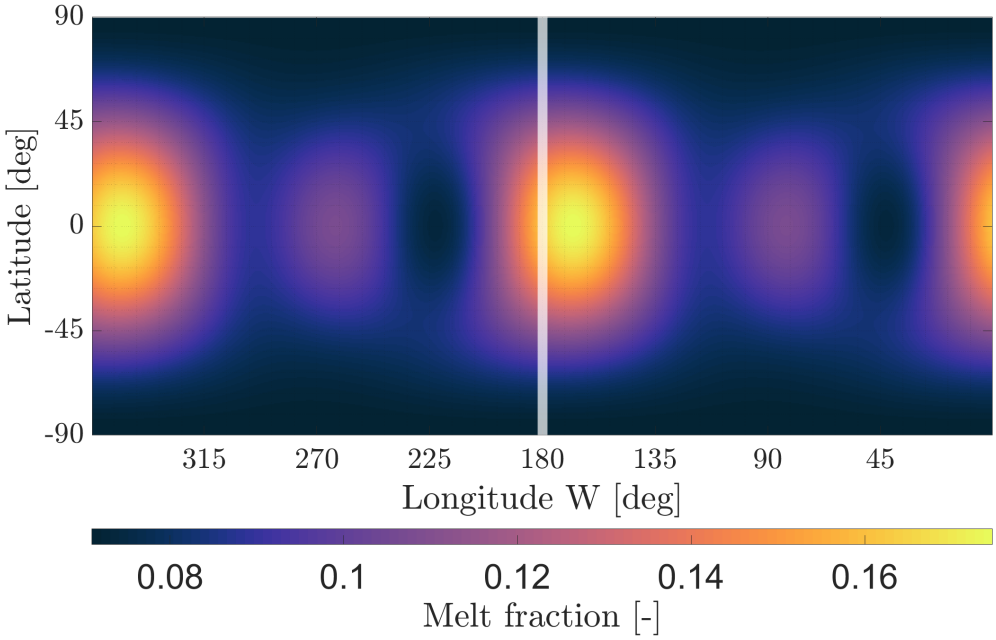


**Fig. A2** Melt fraction resulting from, and causing, the tidal dissipation pattern presented in Fig. 2. The vertical white line indicates 180° W.

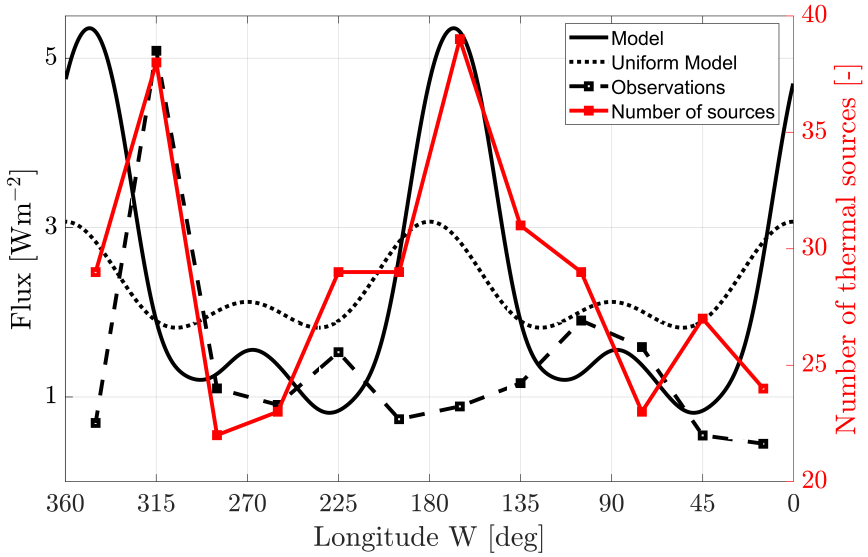


**Fig. A3** Longitudinal heat flux pattern of our model as presented in Fig. 2 together with the observed longitudinal heat flux, and the longitudinal distribution of thermal sources [1].

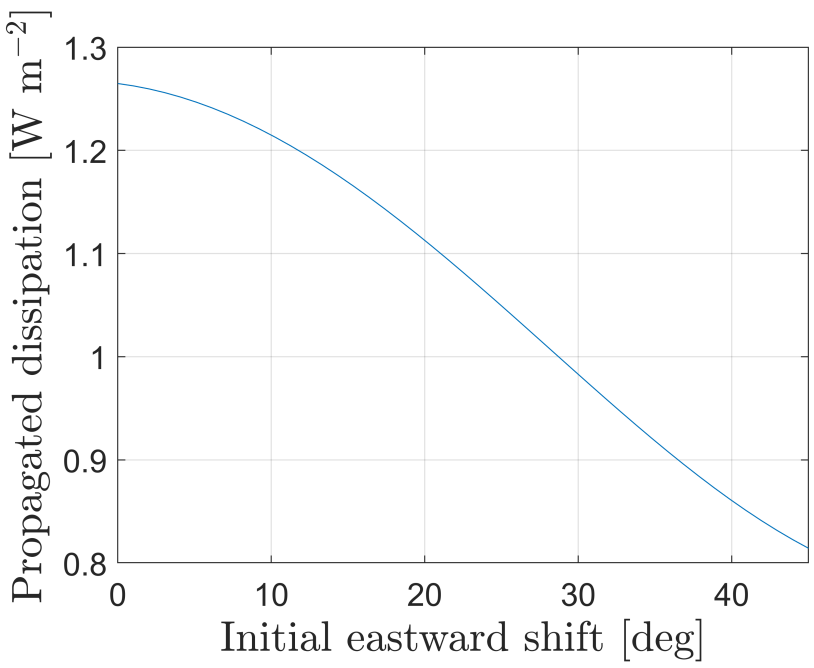


**Fig. A4** The propagated tidal dissipation for varying initial eastward shift at a peak-to-peak lateral variation of 86%

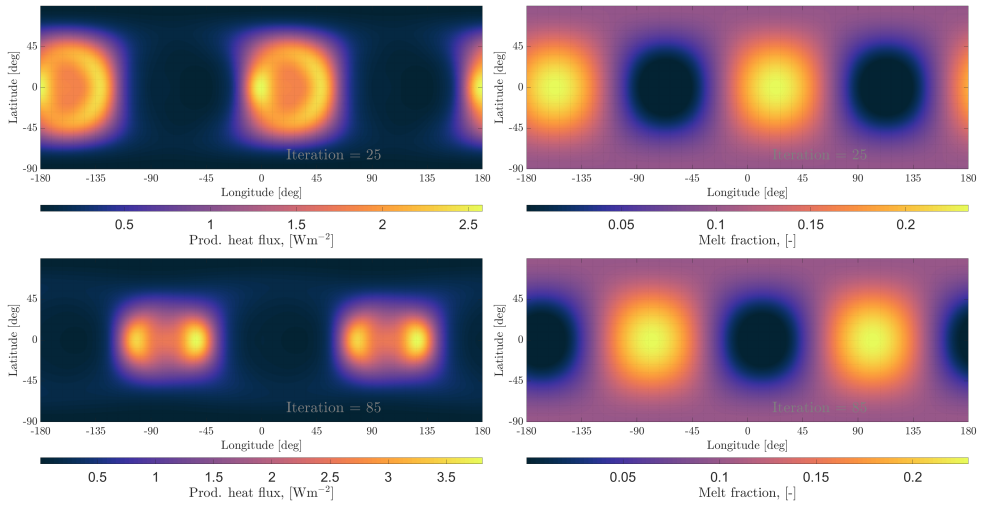


**Fig. A5** Alternating tidal and heat flux patterns that arise for very intense coupling. The top two plots show the surface heat flux and melt fraction patterns when the maximum melt fraction is east of the prime meridian. The bottom two plots are when the maximum melt fraction is just west of the prime meridian. The plots demonstrate that when $c$ becomes too large there is no longer a stable point.

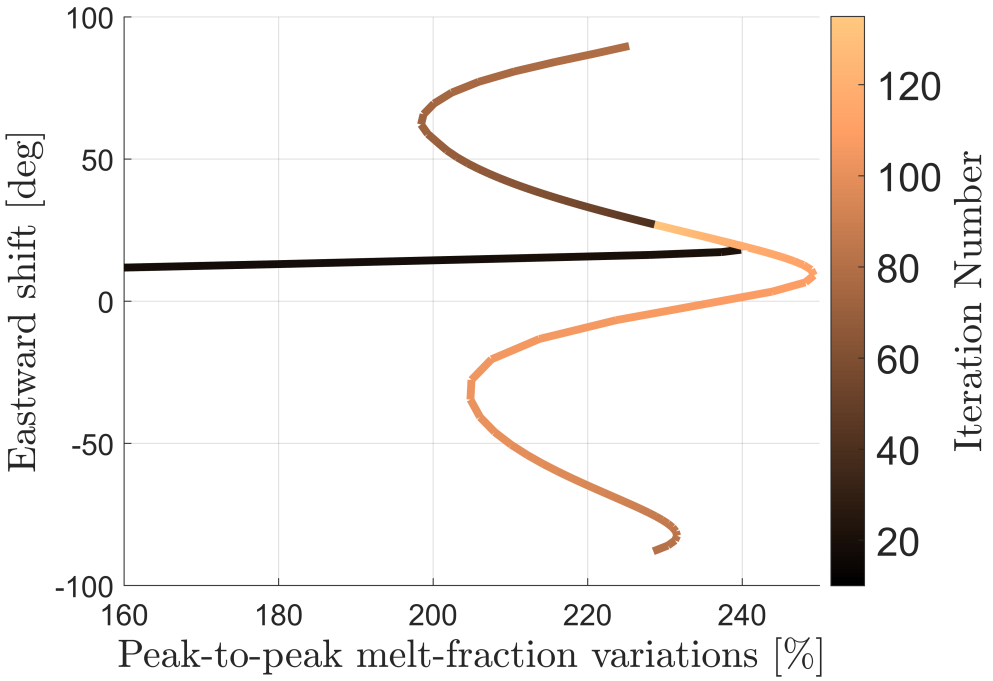


**Fig. A6** The trajectory of the melt fraction pattern, plotted in the same phase-space as Fig. A5, for very intense coupling. The eastward shift with respect to the prime meridian of the degree and order 2 melt fraction mode is plotted against the peak-to-peak melt fraction variations. The color of the line represents the number of iterations.

**Table A1** Model Parameter Values. Values are taken from Segatz et al. [2] and Steinke et al. [3].

| Parameter | Notation | Value | Unit |
|---|---|---|---|
| Orbit eccentricity | $e$ | 0.0041 | - |
| Core-Mantle boundary | $R_{\rm cmb}$ | 965 | km |
| Mantle-Asthenosphere boundary | $R_{\rm m}$ | 1591.6 | km |
| Asthenosphere-Crustal boundary | $R_{\rm ast}$ | 1791.6 | km |
| Mean radius | $R_{\rm Io}$ | 1821.6 | km |
| Core density | $\rho_c$ | 5150 | kg m$^{-3}$ |
| Mantle and crust density | $\rho_m$ | 3244 | kg m$^{-3}$ |
| Mantle shear modulus | $\mu_m$ | $6 \times 10^{10}$ | Pa |
| Mantle viscosity | $\eta_m$ | $10^{20}$ | Pa s |
| Asthenosphere shear modulus | $\mu_{\rm ast}$ | $7.8 \times 10^{5}$ | Pa |
| Asthenosphere viscosity | $\eta_{\rm ast}$ | $10^{11}$ | Pa s |
| Crustal shear modulus | $\mu_c$ | $6.5 \times 10^{10}$ | Pa |
| Crustal viscosity | $\eta_c$ | $10^{23}$ | Pa s |
| Average melt fraction | $\bar{\Phi}$ | 10% | - |

## Comparison with a FEM model

Here, we compare the output of LOV3D with a FEM model [3]. The FEM model is built in ABAQUS using the method described in Wu [4] to account for self-gravitation. The model was initially developed by Hu et al. [5] and later modified by Steinke et al. [3] to apply it to Io. The runs shown here use a grid size of 1° and are split into 19 radial layers: 6 comprising the mantle, 10 for the asthenosphere, and 3 for the lithosphere [6]. The total run time was 4 orbits with 15 timesteps per orbit, and only the last orbit was used to compute the orbital-average tidal heating.

In the comparison, we introduce lateral variations of tidal heating of spherical harmonics degree 2 expected from asthenospheric heating (pattern B in Beuthe [7]) and map them to melt fraction variations as described in the Method and Steinke [6] using

$$\delta\Phi(\theta,\phi) = c\, Q_{\mathrm{ref,obs}} \left( \frac{\Psi_2(\theta,\phi)}{\Psi_0} \right) ,$$

with $c = 0.02$, $Q_{\mathrm{ref,obs}} = 2.3\ \mathrm{Wm}^{-2}$, $\Psi_0 = 21/5$, and

$$\Psi_2(\theta,\phi) = 0.5 \left( -\frac{33}{7} P_{20}(\cos\theta) + \frac{9}{14} P_{22}(\cos\theta)\cos(2\phi) \right),$$

with $P_{20}(\cos\theta)$ and $P_{22}(\cos\theta)$ the degree 2 associated Legendre polynomial of order 0 and 2 respectively. The average melt fraction is 10%. We compute the tidal dissipation with this pattern as input, shown in *a)* of Fig. A7, or the same pattern but shifted eastward by 30 degrees, shown in *b)* of Fig. A7. Both codes used the same interior properties (given in Table A1) and used $B_\eta = 20$ instead of the $B_\eta = 26$ that was used to create the main results of the article.

We found that the mean heat flux predicted by the FEM model is consistently lower than with *LOV3D*. This is also the case for the spherically-symmetric case, for which the spectral model provides the expected average dissipation from semi-analytical models and the FEM underestimates it by roughly 20%. The underestimation of tidal

heating in the FEM models is the result of the coarse model resolution, which cannot capture strong radial gradients in tidal heating in the thin asthenosphere, and the relatively short spin-up phase of the FEM, both required to keep the numerical cost at bay.

As these numerical problems are expected to affect the outcome of both the spherically symmetric model and the one with lateral variations in a similar way, the effect of lateral variations can be better compared using the heat flux normalized with respect to the mean. Doing so, we find excellent agreement between the predictions of the FEM model and *LOV3D*. The output of *LOV3D* is plotted in the top row and since the results are very similar, we do not plot the output of the FEM model but rather the difference between the output of the two codes in the bottom row. What is left is clearly a result of the discretization that the FEM model has to do. The pattern and relative magnitude of tidal heating anomalies caused by lateral variations agree, showing discrepancies of around 5%.

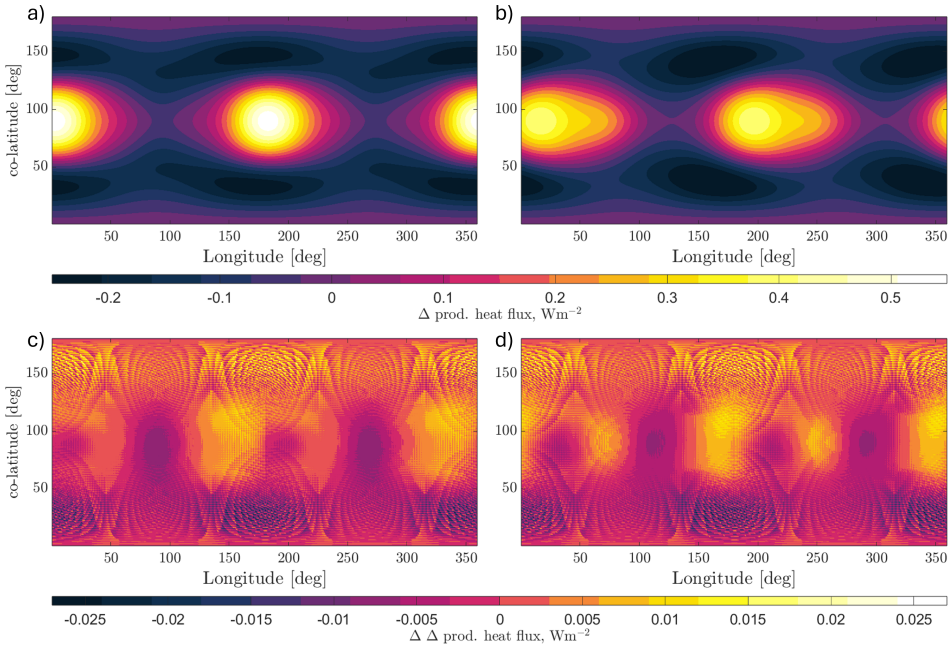


**Fig. A7** Normalized difference in tidal dissipation of an Io with lateral variations compared to that of a uniform Io with a LOV3D and a spectral code. The plots in the top row (a,b) were generated using *LOV3D* and the ones in the bottom row (c,d) are the difference of the top row with respect to the same results generated using a FEM code [6]. The lateral variations used in the plots of the left column (a,c) are centered at the prime meridian while those in the right column (b,d) have their initial melt-fraction pattern shifted eastwards by 30 degrees.

# References


[1] Davies, A.G., Perry, J.E., Williams, D.A., Veeder, G.J., Nelson, D.M.: New Global Map of Io's Volcanic Thermal Emission and Discovery of Hemispherical Dichotomies. The Planetary Science Journal **5**(5), 121 (2024) https://doi.org/10.3847/PSJ/ad4346

[2] Segatz, M., Spohn, T., Ross, M.N., Schubert, G.: Tidal dissipation, surface heat flow, and figure of viscoelastic models of Io. Icarus **75**(2), 187–206 (1988) https://doi.org/10.1016/0019-1035(88)90001-2

[3] Steinke, T., Hu, H., Höning, D., van der Wal, W., Vermeersen, B.: Tidally induced lateral variations of Io's interior. Icarus **335**, 113299 (2020) https://doi.org/10.1016/j.icarus.2019.05.001

[4] Wu, P.: Using commercial finite element packages for the study of earth deformations, sea levels and the state of stress. Geophysical Journal International **158**(2), 401–408 (2004) https://doi.org/10.1111/j.1365-246X.2004.02338.x

[5] Hu, H., Wal, W., Vermeersen, L.L.A.: A numerical method for reorientation of rotating tidally deformed viscoelastic bodies. Journal of Geophysical Research: Planets **122**(1), 228–248 (2017) https://doi.org/10.1002/2016JE005114

[6] Steinke, T.: The Curious Case of Io - Connections Between Interior Structure, Tidal Heating and Volcanism. PhD thesis, Delft University of Technology (2021). Chap. 3. https://doi.org/10.4233/uuid:9e875752-05bc-4dd8-9bdd-77e18cf3c43f

[7] Beuthe, M.: Spatial patterns of tidal heating. Icarus **223**(1), 308–329 (2013) https://doi.org/10.1016/j.icarus.2012.11.020